This is an open access article published under a Creative Commons Attribution (CC-BY) License, which permits unrestricted use, distribution and reproduction in any medium, provided the author and source are cited.

ACS AUTHORCHOICE

ACS Catalysis

pubs.acs.org/acscatalysis

Research Article

Imaging the Heterogeneity of the Oxygen Evolution Reaction on Gold Electrodes Operando: Activity is Highly Local

Gregor Zwaschka,[‖] Igor Nahalka,[‖] Arianna Marchioro, Yujin Tong, Sylvie Roke, and R. Kramer Campen*

Cite This: *ACS Catal.* 2020, 10, 6084–6093

Read Online

ACCESS | Metrics & More | Article Recommendations | Supporting Information

ABSTRACT: Understanding the mechanism of the oxygen evolution reaction (OER), the oxidative half of electrolytic water splitting, has proven challenging. Perhaps the largest hurdle has been gaining experimental insight into the active site of the electrocatalyst used to facilitate this chemistry. Decades of study have clarified that a range of transition-metal oxides have particularly high catalytic activity for the OER. Unfortunately, for virtually all of these materials, metal oxidation and the OER occur at similar potentials. As a result, catalyst surface topography and electronic structure are expected to continuously evolve under reactive conditions. Gaining experimental insight into the OER mechanism on such materials thus requires a tool that allows spatially resolved characterization of the OER activity. In this study, we overcome this formidable experimental challenge using second harmonic microscopy and electrochemical methods to characterize the spatial heterogeneity of OER activity on polycrystalline Au working electrodes. At moderately anodic potentials, we find that the OER activity of the electrode is dominated by <1% of the surface area and that there are two types of active sites. The first is observed at potentials positive of the OER onset and is stable under potential cycling (and thus presumably extends multiple layers into the bulk gold electrode). The second occurs at potentials negative of the OER onset and is removed by potential cycling (suggesting that it involves a structural motif only 1−2 Au layers deep). This type of active site is most easily understood as the catalytically active species (hydrous oxide) in the so-called incipient hydrous oxide/adatom mediator model of electrocatalysis. Combining the ability we demonstrate here to characterize the spatial heterogeneity of OER activity with a systematic program of electrode surface structural modification offers the possibility of creating a generation of OER electrocatalysts with unusually high activity.

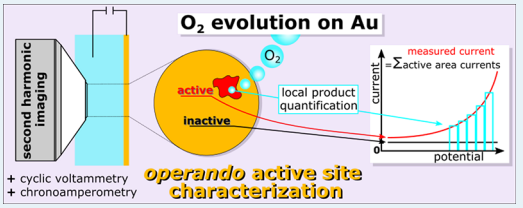

KEYWORDS: *heterogeneous electrocatalysis, oxygen evolution reaction, local activity, operando active site characterization, second harmonic imaging, gold electrodes*

1. INTRODUCTION

It is increasingly clear that a global energy economy based on hydrocarbon combustion has adverse consequences for the climate, the Earth surface environment, and human health. An economy instead based on the combustion of H_2 would avoid virtually all of these consequences. Perhaps the best candidate to produce H_2 sustainably is (photo)electrochemical water splitting (where the large energy input required for the reaction comes from a renewable source). Although finding catalysts that are active, stable, and inexpensive for both halves of this redox reaction is challenging, the oxidation half of water splitting, the oxygen evolution reaction (OER), is currently rate-limiting in most devices.[1] The relative sluggishness of the OER is a kinetic limitation: the high overpotential necessary to drive it is a result of a high activation barrier. In principle, choice of an appropriate electrocatalyst should be able to lower the overpotential. However, the rational design of an efficient OER catalyst is hampered by our incomplete understanding of the reaction mechanism. This lack of understanding is presumably exacerbated by the OER's complexity: it requires the transfer of four electrons and involves an unknown number of corresponding intermediates.

Much past work, principally in gas-phase heterogeneous catalysis, has shown that catalyst surface atomic structure can often be correlated with activity[2]: certain atomic-scale structural motifs outperform others by many orders of magnitude (e.g., steps vs terraces). Quantifying such structure/reactivity correlations is powerful; it makes it possible to infer the identity of catalytically active sites.[3] It is perhaps unsurprising that the identity of the active site depends on the reaction, catalyst, and catalyst surface structure: predicting the active site of a particular catalyst for a particular reaction has proven extremely challenging. Part of the difficulty is that any such prediction requires knowledge of

Received: March 11, 2020
Revised: April 30, 2020
Published: April 30, 2020

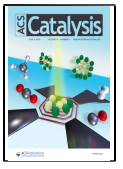

Downloaded via FRITZ HABER INST DER MPI on June 26, 2020 at 07:01:10 (UTC).
See https://pubs.acs.org/sharingguidelines for options on how to legitimately share published articles.

© 2020 American Chemical Society

https://dx.doi.org/10.1021/acscatal.0c01177
ACS Catal. 2020, 10, 6084−6093

the mechanism of the reaction of interest, which may also be a function of the same parameters.

Most studies that have shown clear correlations between surface atomic structure and catalytic activity, whether in the gas phase or electrocatalysis, have done so on single crystals.[4−6] Because surface structure and bonding can be well characterized on such substrates, they are useful systems to demonstrate differences in the activity of terraces and steps for different crystal faces (e.g., (111) vs (100) terraces and/or steps). Such comparisons can be done indirectly by comparing the activity of stepped and unstepped surfaces in an (electro)catalytic experiment[4−6] or directly by operando imaging of the activity of steps and adjacent terraces.[7] While the reactivity of single crystals is not generally of practical interest, some more complex catalysts, e.g., shape-selected supported nanoparticle systems, have reactivities that can be rationalized as a linear combination of the reactivity of the crystal faces of which their surface is composed.[8]

Unfortunately, virtually all candidate electrocatalytic materials have complexity that cannot be straightforwardly understood as a linear combination of features apparent in idealized model systems: e.g., for the great majority of catalysts relevant in industrial contexts, both surface structure and catalytic activity have been shown to be heterogeneous on length scales from nanometers to millimeters.[9] This structural heterogeneity is thought to influence reactivity in at least five ways: (i) grain boundaries (or other microscopic defects) stabilize reactive atomic defects or high step densities that cannot exist on extended surfaces[10]; (ii) differences in local conductivity[11]; (iii) differences in local pK_a[12]; (iv) heterogeneity in transport (e.g., local turbulent flow or nonuniform diffusion); and (v) a resulting spatial heterogeneity in the extent to which the catalyst restructures under reactive conditions.[9] It therefore seems clear that optimizing catalyst performance requires operando imaging of reactivity on the nanometer to millimeter spatial scales of structural heterogeneity. In this study, we meet this challenge by imaging the OER activity and structural heterogeneity of polycrystalline Au electrodes on length scales of 200 nm to 100 μm, which is of particular relevance for this material.

Understanding the OER on noble metals in general and Au in particular is important both for possible application and as a useful model system in OER electrocatalysis. Despite decades of study, neither for the OER nor for the electro-oxidation of Au (which begins at potentials cathodic of and continues through potentials relevant to the OER) does a universally agreed-on picture exist. It is generally accepted that at sufficiently low potentials, the Au surface is covered with anions[13,14] and that, as the potential is scanned increasingly positively, the first step of surface oxidation is the reversible replacement of anions with either O or OH.[1,13−16] While less work exists on the subsequent stages of oxidation, increasing the potential is thought to lead, after completion of the oxygen species monolayer, to site exchange of the oxygen-containing species with gold atoms[17] and the formation of a quasi-three-dimensional hydroxy-oxide film[13,14,18] in which the oxidation state of gold is +3.[19] Koper and co-workers have found that further increasing the potential does not change gold's oxidation state but rather dehydrates the film toward Au_2O_3.[1] This dehydration cannot be complete, however, as pure gold oxide is not stable thermodynamically under oxygen evolution conditions.[20] Regardless of their detailed structure, the first three layers of oxide are typically termed α-oxide and are believed to be compact,[21] while the following layers, termed β-oxide, have been found to be disordered.[19,21] For the actual OER, Koper and co-workers presented evidence from online electrochemical mass spectrometry that the first molecular oxygen is evolved as α-oxide (thought to be formed from the first three layers of Au as one goes from bulk H_2O to bulk Au) and is transformed to β-oxide by a disproportionation of gold hydroxy oxide at 2 V vs. the reversible hydrogen electrode (RHE) in 1 M $HClO_4$.[1] Burke and co-workers also found 2 V vs. RHE to be the onset potential for the OER on Au in a basic electrolyte.[22] At even more positive potentials, other mechanisms for the OER may be active where, for example, one oxygen atom of an O_2 molecule comes from the surface oxide and the other from the electrolyte.[23−25] While the onset potential of the OER on the RHE scale appears to be relatively insensitive to electrolyte pH, much work has clarified that the OER activity is not: most OER catalysts are more active in alkaline media (IrO_x is a notable exception).[26]

This body of prior work clarifies that if we are to understand the spatial heterogeneity of the OER on Au, we also need to understand the spatial heterogeneity of Au surface oxidation: we require an imaging technique sensitive to both processes that can be employed operando. This requirement is nontrivial for at least two reasons: (i) much prior work has clarified that oxidation (and subsequent reduction) lifts the atomic order even for initially well-defined Au single crystals;[15] and (ii) it implies that methods that use electrons as probes (e.g., scanning tunneling microscopy (STM)) or use the optical response of the metal to enhance a photon-based observable (e.g., SEIRAS or SERS) are not applicable.

Here, we apply second harmonic generation microscopy (SHM) to image two different Au electrodes under reactive conditions as Au is oxidized and oxygen bubbles are produced. SHM is a nonlinear optical technique that is surface specific by its symmetry selection rules: we probe here the surface dielectric function with specificity. This surface specificity provides an intrinsic sensitivity to surface processes and allows a precise alignment of the focal plane of the microscope with the Au/electrolyte interface, not possible in linear optical approaches.[27] Using SHM on our Au electrodes under reactive conditions, we find the OER activity to be highly local and to occur in two distinct types of active areas. The first is observed at potentials anodic (i.e., positive) of the OER onset and is stable with respect to surface atom reconstruction during repeated potential cycling. This localization of bubble formation, and its stability with respect to potential cycling, is consistent with a scenario in which bubble formation occurs at a defect that is oxidized and penetrates through the surface into the bulk (potential cycling Au electrodes leads to surface reconstruction of the first two to three Au layers[15]). The relative coverage of the surface with active areas of this type is comparable to the relative coverage of active sites found in gas-phase heterogeneous catalysis, but lower than in other heterogeneous (electro)catalysis studies that probe active sites by indirect means.[a] The current that is passed through this type of active site at potentials anodic of the OER onset can quantitatively explain the measured current across the entire working electrode. The second type of active area is observed at potentials cathodic of the OER onset and is not stable with respect to surface atom reconstruction during potential cycling. This instability is most easily understood if it is the result of a highly active surface motif. Such active sites have been invoked to explain unusually reactive noble metal

https://dx.doi.org/10.1021/acscatal.0c01177
ACS Catal. 2020, 10, 6084−6093

surfaces in a variety of electrocatalytic reactions in the incipient hydrous oxide/adatom mediator model of electrocatalysis.[29−31]

The wide-field imaging of two distinct types of OER active sites on spatially heterogeneous Au offers an essential tool for both fundamental and applied studies: e.g., the systematic dependence of active site distribution on electrolytes and the possibility of engineering Au samples that stabilize few atom layer thin, highly active sites for application in electrolyzers.

2. RESULTS AND DISCUSSION

We initially examined a polycrystalline gold foil working electrode in 0.5 M Na_2HPO_4 (to ensure stable conditions throughout the optical measurements), pH = 9, and collected SH micrographs while conducting linear sweep voltammetry from 1.8 to 2.2 V vs. RHE. The range of the sweep was chosen to start well before oxygen evolution commences (at 2.0 V vs RHE[1]) and to end at a potential where oxygen evolution is fast enough to produce macroscopic O_2 bubbles (as showcased in Figure 1) whose growth rate allows real-time imaging of

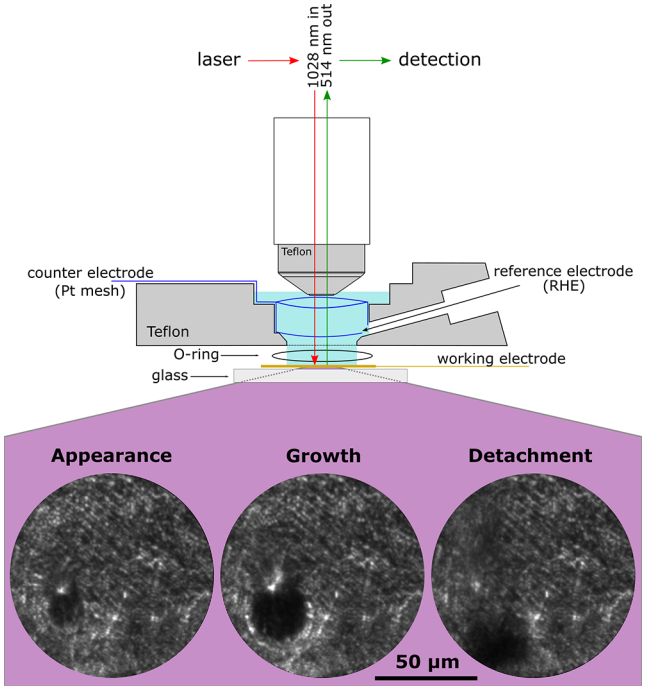

Figure 1. Schematic of the microscopy experiment (top) and life cycle of an oxygen bubble: (bottom left to right) appearance, growth, and detachment as observed in SH micrographs. White (black) indicates higher (lower) second harmonic intensity.

bubble growth and detachment (given the 0.25 s necessary to acquire an image at sufficient signal/noise). The potential sweep is displayed from 1.9 V in the lower panel of Figure 2 in red. In the SH micrographs, structural heterogeneity with a length scale of 10−50 μm is apparent if the potential is kept below the oxidation threshold (see Figure S4 in the Supporting Information for results). Ex situ scanning electron microscopy (SEM) micrographs show structural heterogeneity on similar length scales (see Figure S1 in the Supporting Information), implying that we observe the metal's grain structure in our SH micrographs.

At potentials above oxidation, the different domains can no longer be distinguished clearly and SHM images appear almost featureless, as shown for 1.8 V in the top panel of Figure 2.

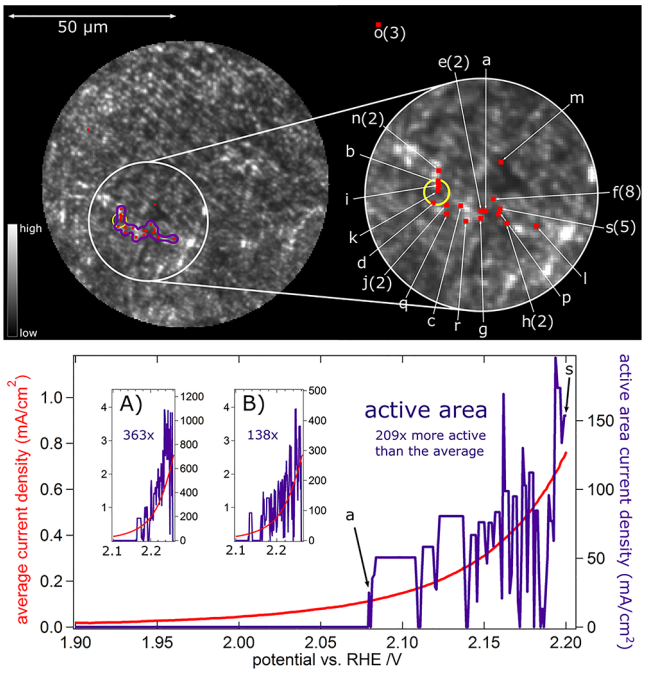

Figure 2. Top-left panel: circular field of view (FOV) of the electrode at 1.8 V vs. RHE in our SH microscope. As shown in the scale bar, white (black) indicates high (low) SH intensity. Red dots indicate sites at which O_2 bubbles nucleated during the linear potential sweep shown in the bottom panel. On the top right, a magnified excerpt is shown that contains nearly all nucleation sites/red dots. The letters assigned to the dots designate the order in which bubbles appeared from the respective spots during the potential sweep. The number in brackets denotes the amount of O_2 bubbles that emerged from each site. The yellow circle denotes the area from which the first O_2 bubbles emerged when repeating the experiment after potential cycling. The bottom panel shows the current density of the average electrode (in red) and the active area (in purple, calculated as discussed in the text) as a function of potential during a linear sweep from 1.9 to 2.2 V vs. RHE with a sweep rate of 1 mV/s. "a/s" denotes the first/last bubble, as in the top-right panel. Insets (A) and (B) show comparable current density vs. potential plots for two more spots on the same surface that were the sole active areas in different FOVs during repeated experiments. The electrolyte was 0.5 M Na_2HPO_4.

However, as the potential is scanned increasingly positively bubbles appear, grow, and detach from the electrode. On the top left of Figure 2, the entire field of view is displayed as a grayscale image with red dots indicating sites of O_2 bubble formation above 2.0 V vs. RHE. The half width at half-maximum spatial resolution of our microscope is 188 nm.[12] As a result, we approximate the site of bubble formation, i.e., determine where to plot the red dots, by examining the first frame in which a spherical bubble could be clearly discerned from the background and taking the center of the circle as the bubble nucleation site (red dot). The bubble radius at this point was approximately 3 μm (see Section S8 of the Supporting Information for a detailed discussion of the nucleation radius of a bubble). As is apparent from Figure 2, the vast majority of bubbles appear within a highly confined active area encircled in purple.

As is evident from the figure, in a single potential sweep at some spots only a single bubble appeared, while in others, multiples appeared either in direct succession or with a pause in between. With increasing potential oxygen bubbles start to

https://dx.doi.org/10.1021/acscatal.0c01177
ACS Catal. 2020, 10, 6084−6093

appear at more spots. Inspection of the data in Figure 2 clarifies that the first bubble we observe is 0.07 V higher in potential than the onset of the OER at 2 V. This offset can be rationalized if the low current densities close to the onset potential indicate an O_2 formation rate insufficient to locally supersaturate the electrolyte with O_2.

While the series of SH micrographs show that bubble appearance is strongly localized, they do not demonstrate whether the activity is localized: whether the current flow necessary to explain bubble production is a significant portion of the measured current flow through the whole electrode. To make this comparison, we estimate the number of O_2 molecules necessary to explain the observed bubbles by measuring the diameter of each bubble in the frame that it detaches from the surface, assuming that the bubble is formed of 1 atm of O_2 and using the ideal gas law. We then compare this estimated bubble-related current to the current expected to flow through the FOV based on measurement of the whole electrode. If the current necessary to produce the O_2 bubbles we observe is large with respect to that expected based on the measured current over the whole electrode and the size of our field of view, it suggests that O_2 generation that does not result in bubble formation and Au oxidation do not contribute significantly to the measured electrode current. For the results shown in Figure 2, this condition is clearly met: under these conditions for the series of micrographs shown in the main panel, inset A and inset B, the current required to generate the bubbles is 188, 195, and 134% of the current expected to flow through an area the size of the field of view, respectively. Clearly, under the conditions of this linear sweep voltammetry, current flow is dominated by electrochemical oxygen evolution resulting in bubble formation.

The local, high, density of sites at which oxygen bubbles appear can be rationalized as the result of either transport or chemistry: we observe either an active area for bubble nucleation from a neighboring electrolyte supersaturated in O_2 or an active area for O_2 generation. As we show in detail in Section S6 of the Supporting Information, the high time resolution of our approach allows us to finely resolve the bubble growth rate and to show that its time dependence is incompatible with a diffusion-limited scenario (growth rate does not scale with the bubble surface area). The fact that the bubble growth rate is independent of the bubble surface area suggests that for bubbles of radius 3 μm and larger, the O_2 responsible for bubble growth is produced locally: the active areas we observe, on the micrometer length scale, are active with respect to O_2 generation.

Much prior work suggests that the bubbles we observe nucleate at length scales much smaller than those accessible in our microscope. For example, White and co-workers have extensively studied electrochemically generated nanobubbles of a variety of gasses, i.e., H_2, N_2, and O_2, on Pt nanoelectrodes as well as on microelectrodes in confinement.[32−35] These studies suggest that, on Pt nanoelectrodes, bubble nucleation occurs with a critical size as small as 4−5 nm[36] and is driven by a strong supersaturation of the electrolyte close to the electrode with the respective gas (up to 300 times larger than the saturation concentration under standard conditions[37]) rather than local differences in activity. Works by others suggest that the necessary degree of supersaturation is extremely sensitive to details of the surface: for larger Pt microelectrodes, the reported supersaturation values for nucleation ranged from 1.5 to 24 times standard concentrations.[38,39] For other surfaces, the formation of surface nanobubbles without supersaturation of the electrolyte with gas has been reported.[40,41]

Clearly, the 4−5 nm length scale of bubble nucleation is not observable in our SH microscope, and thus it is difficult to draw conclusions about the nucleation and growth mechanism. Our results are consistent either with a scenario in which the nucleation of O_2 bubbles occurs inside of nanopores on the surface that enabled local supersaturation of the electrolyte with O_2 even at minute current densities (e.g., 0.11 mA/cm^2 during the observation of bubble A in Figure 2) or one in which on our macroscopic electrode a much lower supersaturation is required due to heterogeneous nucleation at structural motifs that are active sites with respect to bubble nucleation and are larger than the electrodes used by White et al., e.g., grain boundaries. Regardless of the mechanism of bubble nucleation, however, as soon as bubbles are large enough to be observed in our microscope, we find bubble growth to be driven not by mass transport from solution via diffusion but by local electrochemical O_2 evolution.

To quantify the reactivity of these active areas with respect to the OER, we require a current density. For this purpose, we calculate the current necessary to explain the observed bubble formation as described above and obtain a current density by dividing it by the geometric surface area of the active area, 69.9 μm^2 in the case of the data shown in the main panel of Figure 2 (see the Supporting Information Section S8 for a detailed description of the calculation of the surface area and the sensitivity of our results to the method we employed). The resulting current density is plotted in the lower graph as a purple curve starting with point **a** around 2.07 V vs. RHE and is denoted "active area current density". Its increase with potential correlates well with the potential-dependent behavior of the average electrode (red curve), but its current density is significantly higher. Integrating the current density from the active area over the course of the experiment (from **a** to **s**) and comparing it to the integrated current density of the entire electrode (during the same period), we find that the active area's charge density is 209 times higher than the electrode average. This similarity in the change in current density with potential of the active area and measured electrochemical current density is shown for two more spots in different positions of the electrode, monitored individually by SHM in repeated experiments, as insets. The integrated current densities of the active areas corresponding to the two insets are 363 (A) and 138 (B) times higher than the electrode average.[b] Assuming that the FOVs we measure are representative of the electrode as a whole, the active areas in Figure 2 are 138−363 times more active than the electrode average and the measured current results from 0.28 to 0.72% of the area of the electrode.

While the molecular-level structure of an active site is substrate- and reaction-dependent for both electro- and gas-phase catalyses, our estimate for the fractional coverage of the surface with active areas (0.28−0.72%) compares well with active site coverages from gas-phase catalysis studies but is considerably lower than ex situ estimates of active site coverages in electrocatalytic systems. Studies on gas-phase catalysis, e.g., the catalytic dissociation of NO[42] and N_2[43] on well-defined single crystals and propene metathesis on less-well-defined metal oxides,[44] find active site coverages of 1−2%. The similarity of these estimates to our 0.28−0.72% active area is consistent with our conclusion that we observe active sites for O_2 generation. In contrast, previous estimates for the

https://dx.doi.org/10.1021/acscatal.0c01177
ACS Catal. 2020, 10, 6084−6093

fraction of active sites on Au electrocatalysts for hydrogen evolution, determined from the spontaneous deposition of Ag, Pd, and Pt at active sites to poison the surface, find 5[45,46] to 7[47]% of the surface to be active. In part, these differences in active site coverage may be the result of the means of characterization: while in the electrocatalysis studies, active site coverage was determined by ex situ methods, both in our and in the metathesis study, active site coverages were determined operando. Prior work, much of it on gas-phase catalytic chemistry, has emphasized the importance of operando active site characterization because active sites evolve[48,49] or even only appear[9] under reaction conditions. As described above, prior work characterizing active site abundances in electrocatalysis is largely either indirect, i.e., inferred from current voltage measurements of well-defined single-crystal surfaces, or ex situ, i.e., measured by mass spectrometry of adsorbed metal offline. Our SH imaging of active sites overcomes both of these shortcomings.

Having observed an active area for electrochemical oxygen production and O_2 bubble formation, we next investigated this area's stability. As has been demonstrated by prior authors in a variety of electrochemical STM studies, cycling the bias across an Au electrode between 0 and 1.7 V vs. RHE, i.e., repeatedly oxidizing and reducing the surface, results in surface reconstruction.[15] While the extent of reconstruction is a function of scan rate and time spent at oxidizing potentials, current features that persist after such cycling are presumably related to structural motifs that are insensitive to surface reconstruction. Put another way, if the activity of the active area was the result of a specific arrangement of surface atoms only, one might expect that the active area for bubble generation would shift with every oxidation/reduction cycle. Repeating the experiment after restructuring the electrode surface yields bubble growth from the same active area: the yellow ring shown in the upper panel of Figure 2. Given that O_2 bubble formation only starts close to 2.1 V vs. RHE, our data are thus consistent with a scenario in which highly active sites for the OER on this intermediate-complexity Au electrode are the result of an oxidized structural defect penetrating into the bulk.

The polycrystalline Au foil makes the validation of this conclusion challenging: we do not know from the SH micrographs how deeply this structural feature might penetrate and, as discussed above, we expect that the structural character of the active area is likely to change under ex situ conditions (where, for example, one might imagine investigating the depth-dependent electrode structure by focused ion beam milling and subsequent scanning/transmission electron microscopy). Instead, we approach this problem from the sample side. That is, we also examined a gold electrode obtained by physical vapor deposition of gold on an optically smooth glass surface. This electrode is mirror smooth and comprises ~50 nm clusters (see Figure S2 in the Supporting Information for an SEM micrograph of the as-prepared sample). After positioning the microscope FOV over a surface defect, we ramped the bias from 0 to 2.3 V vs. RHE with a scanning speed of 60 mV/s and then held it at 2.3 V for 2 min. The FOV including the defect is shown in the top left, a view of the forming bubble on the upper right, and the measured current (inferred from the microscope FOV and the area of the working electrode) and integrated SH intensity both on and off the defect on the lower half of Figure 3.

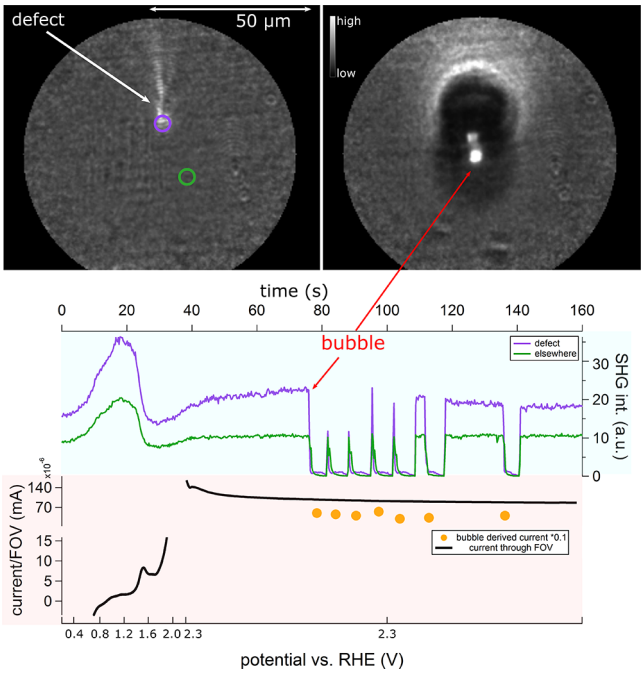

Figure 3. Top-left panel shows the circular FOV of a physical-vapor-deposited gold electrode at 2.3 V vs. RHE, including a defect, as observed with our SH microscope. The same view is shown on the right, including an oxygen bubble forming from the defect. As shown on the scale bar, white (black) indicates high (low) second harmonic intensity. The lower half of the bottom panel shows the current passing through the FOV (calculated from the size of the FOV versus the geometric area of the electrode) during the linear potential sweep up to 2.3 V and the potentiostatic experiment at 2.3 V in black together with the current that is passed to form bubbles after 75 s in orange. The upper half of the lower panel shows the SH intensity on and away from the defect. The scanning speed of the linear sweep was 60 mV/s, and 0.5 M Na_2HPO_4 was used as the electrolyte.

The measured current clarifies that scanning the bias from 0 to 2.3 produces the expected oxidation current feature at 1.5 V vs. RHE: from an electrochemical point of view, the surface is clearly oxidized when it reaches 2.3 V. The upper half of the lower panel of Figure 3 shows the average SH intensity per pixel for areas on and away from the "defect". Two characteristics of these curves are evident from inspection: (a) both increase up to the oxidation current peak and decrease rapidly thereafter and (b) the SH intensity on the defect appears to be offset positively from that in the surroundings. Both observations are consistent with previous literature: for a wide variety of Au electrodes and electrolytes, the SH intensity has been observed to increase with increasing potential up to oxidation and decrease thereafter,[50,51] while, at a given potential, the SH intensity on Au has been found to be a function of the surface structure and even of the azimuthal angle for a given surface structure.[52] It is worth emphasizing that because the SHG intensity is a sensitive probe of surface dielectric function, the qualitatively identical change in the SHG intensity with potential on and off the defect strongly suggests that the defect is composed of Au and not a contaminant.

As shown in Figure 3, after the bias reaches 2.3 V vs. RHE, the sample was maintained under potentiostatic control. Under these conditions the measured current is constant, the integrated I_{SH} off the defect is also constant, and that on the

https://dx.doi.org/10.1021/acscatal.0c01177
ACS Catal. 2020, 10, 6084−6093

defect slowly increased. While understanding this potential-induced change in local SH contrast is challenging, the different behavior is most easily rationalized if under these electrochemical conditions the local structure near the defect continues to evolve while that away from the defect is stable. Thirty-six seconds after the potential was fixed at 2.3 V vs. RHE, bubbles start to emerge at the defect. As these bubbles grow, detach, and diffuse out of the field of view, the local SH signal decreases due to scattering and then recovers as the bubble diffuses away. The frame in which the first bubble detaches is shown in the top right of Figure 3. The first five bubbles emerge from the defect in rapid succession with no waiting period in between. Between bubbles five and six, there is a waiting period of ≈5 s. Between bubbles six and seven, this waiting period grows to almost 20 s. The SH intensity on the defect during the waiting periods and after bubble seven decreases with respect to its value before the first bubble. The current passed to create the bubbles is shown as orange dots in the lower panel, and the current passed through the FOV as the reference is shown in black. As expected for these potentiostatic conditions, the current is approximately constant. In contrast to the polycrystalline Au electrode shown in Figure 2, here the bubble estimated current exceeds the expected current for an area the size of the FOV (based on the measured current from the whole electrode) by 10× (bubble derived current is scaled by 0.1× to fit on the same plot). This result reflects that these defects are relatively uncommon on the PVD sample, i.e., the great majority of FOVs we observed did not have them, and thus the FOV showing the data in Figure 3 is not representative of the electrode as a whole.

The increase in waiting time and the decrease of the signal intensity on the defect after the fifth bubble are consistent with a scenario in which the structure of the active area evolves and its reactivity decreases under OER conditions. The former conclusion is consistent with the results of much prior work (although only through indirect means at solid/liquid interfaces): catalyst active sites are dynamic under reaction conditions.[48,49,53] We rationalize the apparent decrease in reactivity by noting that the OER on Au is known to occur on an increasingly oxidized surface, and the thermodynamic driving force for production of O_2 by lattice disproportionation of the metal oxide is larger than that of O_2 production from water splitting.[20] Together with the observation that metal corrosion accompanies the OER,[54] the data displayed in Figure 3 are thus consistent with a scenario in which the OER at 2.3 V vs. RHE consumes catalytically active, partially oxidized Au cations more quickly than they are created.

We also observed a second type of dynamic active area behavior qualitatively different from that shown in Figure 2 on the polycrystalline Au electrodes. This type of active area differs from that described previously in two ways: (i) they are sites at which oxygen bubbles appear at potentials lower than 2 V vs. RHE and (ii) they disappear after potential cycling (presumably they are not stable with respect to potential-induced surface reconstruction). A representative series of experiments is shown in the left panel of Figure 4. Here, repeated cyclic voltammograms (CVs) were collected, using the polycrystalline electrode of Figure 2 but monitoring a different spot with SHM, between a lower limit of 0 V vs. RHE and an upper limit that started at 1.6 V and increased to 2.05 V vs. RHE in steps of 0.15 V. In experiment 1, for example, an O_2 bubble was produced in the penultimate cycle at 1.9 V and in

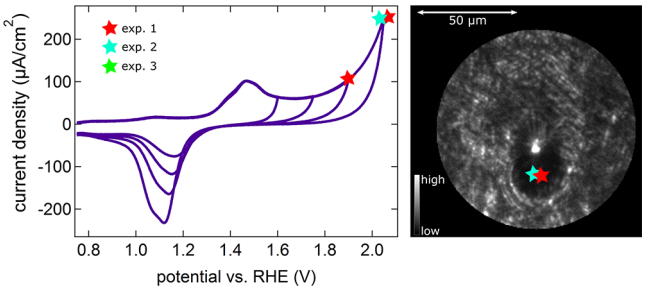

Figure 4. Left panel: cyclic voltammograms collected in three separate experiments on the polycrystalline Au electrode also used in Figure 2. In each experiment, four CVs are collected in the following order: 0−1.6, 0−1.75, 0−1.9, and 0−2.05 V vs. RHE. For all CVs, the scan rate was 60 mV/s, and 0.5 M Na_2HPO_4, pH = 9, was used as the electrolyte. The right panel shows the formation of a bubble during the experiment. The SH micrograph shown was collected during experiment 1 at 1.9 V vs. RHE. The nucleation sites during experiments 1 and 2 are shown as colored stars. The FOV was different from the three fields of view summed up in Figure 2.

the last cycle at 2.05 V vs. RHE. The potentials at which bubbles were produced are marked in the respective voltammogram by stars that have a separate color for each experiment. In experiment 2, a bubble was only produced at 2.05 V. Experiment 3 and following cyclic voltammetry experiments did not yield bubble growth at all. On the right of Figure 4, the production of a bubble in experiment 1 is shown together with stars in red and turquoise, which indicate the location of bubble nucleation. This behavior is unexpected; prior empirical work[1] and our findings discussed above suggest that O_2 should be generated on polycrystalline Au only anodic of 2 V vs. RHE. The observation of O_2 bubble formation under conditions in which the electrode as a whole is clearly not active with respect to the OER is the most easily understood if the areas indicated are active with respect to electrochemical O_2 production. That is, the observation of bubbles forming on these sorts of dynamic active areas is extremely unlikely to be the result of just bubble nucleation from a supersaturated solution.

In chronoamperometric experiments analogous to the experiments shown in Figure 3, but at a potential of 1.9 V vs. RHE (i.e., also before the expected onset of the OER), formation of a single bubble per experiment was observed in two successive experiments, but not subsequently. The bubbles formed in the chronoamperometric and cyclic voltammetry experiments originated from spots that lie outside the active area of Figure 2. Corresponding SH count versus potential curves, which show the signature of bubble formation, can be found in Section S10 in the Supporting Information.

Given the body of prior work discussed earlier, and our results shown in Figures 2 and 3, Au oxidation is clearly a prerequisite to O_2 evolution. The metastable active sites shown in Figure 4 are consistent with a scenario in which high-energy, high-reactivity sites exist on our polycrystalline Au that are oxidized and begin to emit O_2, at potentials cathodic of O_2 evolution observed by both us and others on more homogeneous surfaces.[1] Because these sites appear to be largely removed on voltammetric cycling, such defects are likely surface-bound. Oxygen evolution from such transient surface sites, 200 mV before the regular onset of the OER, has previously been observed, indirectly, by Burke et al.[55]

https://dx.doi.org/10.1021/acscatal.0c01177
ACS Catal. 2020, 10, 6084−6093

Despite being the noblest of metals and relatively inert with respect to chemisorption, Au electrodes show surprising activity in a variety of oxidation and reduction reactions.[22] Burke and co-workers hypothesized that this activity could be explained by the presence of surface-bound undercoordinated metal species (adatoms, clusters) that are oxidized at potentials substantially below that of the bulk metal. The result of this premonolayer oxidation, a minority species called "incipient hydrous oxide", is argued to be the catalytically active entity of Au and noble metal electrodes in general, for a wide variety of different reactions.[29] To correlate the presence of the incipient hydrous oxide with catalytic activity, electrode pretreatment protocols to increase the abundance of this minority species (until they were no longer a minority species) were designed that allowed these authors to observe anodic features in the bilayer region of the first CV scan that were assigned to the formation of the incipient hydrous oxide (which is structurally distinct from α- and β-oxides).[30,31] Surfaces with stronger anodic features in the bilayer region showed an increased catalytic activity. Taken together, these experiments suggested what Burke and co-workers termed an "incipient hydrous oxide/adatom mediator" (IHO/AM) model of noble metal electrocatalysis. Such a pretreatment also significantly enhanced the oxygen gas evolution from transient sites at around 1.8 V vs. RHE,[55] linking the IHO/AM model also to fully oxidized surfaces and the OER. This correlation can be rationalized by asserting that either the incipient hydrous oxide persists at higher potentials on an oxidized surface or the surface structure that produces the adatom (that is oxidized to form the incipient hydrous oxide) becomes catalytically active when oxidized or produces a catalytically active oxide at higher potentials.

As noted above, the approach of Burke and co-workers to characterize this incipient hydrous oxide was indirect: the electrode structure was perturbed sufficiently such that a minority species becomes a majority, and the presence of this species was apparent in electrochemical observables. This approach greatly complicates insight into what the high-energy sites actually are or which underlying structure produces them. Our imaging approach circumvents this problem by virtue of its local character: we characterize the transient reactivity of surface species with extremely low coverage. In the case of the first produced bubble in experiment 1 of Figure 4, the current at 1.9 V vs. RHE is on the same level as for the monolayer oxidation and no oxygen evolution would be expected, yet we are able to detect local oxygen production. The production of a bubble under conditions in which no clearly assignable OER current is apparent from voltammetry is consistent with the presence of such transient strongly catalytically active sites on our electrode. Current work in our laboratories focusses on connecting the potential-dependent local Au oxidation signal, apparent in the SH micrographs, to these transiently OER active sites. Such a connection would clarify the nature of this incipient hydrous oxide and its connection to the bulk electrode oxidation.

From a more practical point of view, the observation of OER activity high enough to produce a macroscopic bubble 100 mV prior to the onset of continuous anodic current at 2 V vs. RHE (even under potential cycling at 60 mV/s, i.e., a relatively short period of high anodic polarization), on what presumably is a highly active surface defect, demonstrates the possibility of highly active catalysts that are only a few (1−3) atomic layers thick. Clearly, higher spatial resolution probes, and subsequent physics-directed electrode engineering to stabilize these sites, would be of great benefit in enhancing the kinetics of a variety of electrocatalytic processes. Even at potentials positive of >2 V vs. RHE under a continuous anodic current flow, however, the observation of stable active sites implies that the creation of Au electrodes with defects that penetrate deeply into the bulk (either by mechanical modification or controlling grain boundaries) would strongly enhance the catalytic activity and thus be of great potential importance.

3. SUMMARY AND CONCLUSIONS

In this study, we characterized heterogeneous polycrystalline gold foils with a grain size of tens of micrometers and gold electrodes composed of 50 nm clusters grown by physical vapor deposition (PVD) with second harmonic generation microscopy (SHM) while performing voltammetry and chronoamperometry in pH = 9, 0.5 M Na_2HPO_4. The use of SHM enabled us to directly identify and characterize active sites/areas operando at the interface of an oxidized, nonideal electrode and a liquid phase. At potentials positive of the onset of the oxygen evolution reaction (OER), we observed that the evolution of O_2 bubbles is restricted to small, tens of square micrometers and 0.28−0.72% of the total electrode surface area, but highly active areas on the polycrystalline foil. The current required for O_2 bubble formation quantitatively explains the current we measure over the entire electrode over a range of moderately anodic potentials. Our finding of the relative area covered by active sites is consistent with prior in situ and operando work in gas-phase catalysis but considerably lower than the active site estimate for electrocatalysts from ex situ studies. Because understanding the relationship of local oxidation and O_2 bubble formation on heterogeneous Au foils is challenging, we conducted similar experiments on a PVD gold sample at a potential high enough for a steady-state OER current but low enough to avoid widespread bubble formation on the smooth surface. In this bias window, only at a single defect (that was stable with respect to repeated surface atom rearrangement during electrochemical cleaning) and after the formation of a sufficiently thick oxide layer did bubbles appear. The results of both experiments suggest that this class of highly active areas/active sites for the OER on gold needs a structural defect penetrating to the bulk and a sufficiently thick layer, or specific type, of oxide to form. Finally, in a third type of experiment, the production of O_2 bubbles was observed on the polycrystalline foil at potentials below the onset of the OER in active areas that were unstable under potential cycling. Such metastable active sites are consistent with those suggested by Burke and co-workers previously as the catalytically active entity in the incipient hydrous oxide/adatom mediator (IHOAM) model of electrocatalysis.

Our study is, to our knowledge, the first to describe the spatial heterogeneity of an electrocatalytic reaction at the electrode/aqueous electrolyte interface under reaction conditions through wide-field imaging of product formation. Because of its practical importance and significance for a variety of applications, we studied the electro-oxidation and OER on polycrystalline Au. While the spatial resolution of the microscope precludes molecular-level structural insight into the composition of the active sites and, presumably nanometer scale, bubble nucleation, our results clearly suggest that a combined program of higher resolution, near-field, operando microscopy and systematic electrode modification holds out

https://dx.doi.org/10.1021/acscatal.0c01177
ACS Catal. 2020, 10, 6084−6093

the hope of understanding the relationship of surface structure and active site abundance (in the frame of the IHOAM model of electrocatalysis) and in doing so creating Au electrodes with dramatically enhanced reactivity. The particular issues we address in this study, separating the spatial heterogeneity of oxidation and the OER on Au, are obstacles in the optimization of essentially all practical OER catalysts. As a result, and because the operando SHM approach we describe is not restricted to Au or electro-oxidation/OER (another important application is the investigation of bubble formation and surface wetting behavior of bubbles in water electrolyzers[56]), we expect this study to be of wide interest.

4. EXPERIMENTAL SECTION

4.1. Electrochemistry. A homebuilt Teflon cell was used for the microscopy experiments under potential control. The cell was cleaned by immersion in Piranha solution overnight and repeated supersonication in Milli-Q water before the experiment. Details of the cleaning procedure can be found in our previous work.[57] The Na_2HPO_4 solution was prepared from Fluka Analytical sodium phosphate dibasic (≥99.999%) and Milli-Q water. The polycrystalline gold foils were purchased from Sigma-Aldrich (0.025 mm thickness, 99.99% trace-metal basis) and annealed at 500 °C for 2 h (with linear heating and cooling ramps) to achieve a grain size distribution characteristic of many practically relevant catalysts and suitable for our microscope. The homogeneous gold thin-film sample was obtained by physical vapor deposition of 200 nm of gold on an optically flat glass substrate with a 30 Å layer of Cr for increased adhesion. Before use both electrodes were cleaned using the following procedure: copiously rinsed in acetone, copiously rinsed with Milli-Q water, exposed to ozone for 5 min in a UV ozonator, copiously rinsed with Milli-Q water, copiously rinsed with electrolyte, and annealed electrochemically until the CV was stable (generally 20−30 cycles of cyclic voltammetry). After this procedure, no organic contamination is apparent in the CV (see Figure S3 in the Supporting Information). The counter electrode was a Pt mesh, which was cleaned identically to the Teflon cell. A self-made reversible hydrogen electrode was employed as reference.[58]

4.2. Second Harmonic Wide-Field Microscopy. The light source for the second harmonic microscope is a Pharos SP-1.5 (Light Conversion) laser, which delivers 180 fs pulses centered around 1030 nm at a maximum output power of 6 W and variable repetition rates between 1 kHz and 1 MHz. In this study, the laser system is operated at a repetition rate of 200 kHz. All microscope mirrors on the path are protected silver mirrors (Thorlabs, PF10-03-P01). The lenses (achromatic) and the other optical elements on the illumination path (1030 nm) are near-infrared antireflection coated (Thorlabs, B), while the optical elements on the detection path (515 nm) are antireflection coated for the visible region (Thorlabs, A). We use a spatial light modulator (Holoeye Pluto-NIR-015), which is a phase-only device coated for near-infrared wavelengths, to modify the illumination laser beam, which later on passes through a water immersion microscope objective to illuminate the sample in a wide-field configuration. The illumination objective (Olympus, LUMPFLN 60XW) has 60-times magnification with numerical aperture NA 1.0 and a working distance of 2 mm. This objective illuminates the sample at 34° with respect to the surface normal in a one-beam reflection geometry. The laser is set to deliver a constant fluence of 3.4 mJ/cm^2 at the sample; the diameter of the fundamental beam is 82 μm at full width at half-maximum. The position of the sample is manipulated by an XYZ translation stage (Asi Imaging, PZ-2000), where the *XY*-axes are controlled by actuators with a 10 cm travel range, while the *Z*-axis is moved by a piezoelectric stage with a 300 μm travel range. To extend this positioning system, the microscope objective is mounted on a *Z*-axis actuator stage (Asi Imaging, LS-200). Once the second harmonic photons are generated, they are collected by the same microscope objective used for illumination and further projected on a back-illuminated electron-multiplied and intensified charge-coupled device (CCD) camera with 512 × 512 pixels (PI-MAX4: 512EM-HBf P46 GEN III).

■ ASSOCIATED CONTENT

Supporting Information

The Supporting Information is available free of charge at https://pubs.acs.org/doi/10.1021/acscatal.0c01177.

SEM micrographs of the polycrystalline and PVD Au working electrodes, details of the processing of the SHM images, full cyclic voltammograms along with spatially integrated SH intensity, SH micrographs at potentials below oxidation together with SHG intensity vs. potential curves in different spots, details of bubble identification and size measurement, comparison of observed bubble growth rates to those expected if bubbles were the result of diffusion of O_2 from a supersaturated solution, estimation of the current associated with oxide formation and Au dissolution during bubble growth, determination of the geometric area of the active area, a 2D plot of the correlation coefficient of the averaged FOV SH intensity vs. potential curve with the SH intensity vs. potential curve of every single pixel, SH intensity vs. time curves for cyclic voltammetry and chronoamperometry experiments demonstrating bubble formation below 2 V vs. RHE (PDF)

■ AUTHOR INFORMATION

Corresponding Author

R. Kramer Campen − *Fritz Haber Institute of the Max Planck Society, 14195 Berlin, Germany; Faculty of Physics, University of Duisburg-Essen, 47057 Duisburg, Germany;* orcid.org/0000-0002-7091-2991; Email: campen@fhi-berlin.mpg.de

Authors

Gregor Zwaschka − *Fritz Haber Institute of the Max Planck Society, 14195 Berlin, Germany*

Igor Nahalka − *Laboratory for Fundamental BioPhotonics, Institutes of Bioengineering (IBI) and Materials Science and Engineering (IMX), School of Engineering (STI), and Lausanne Centre for Ultrafast Science (LACUS), Ecole Polytechnique Fédérale de Lausanne, 1015 Lausanne, Switzerland*

Arianna Marchioro − *Laboratory for Fundamental BioPhotonics, Institutes of Bioengineering (IBI) and Materials Science and Engineering (IMX), School of Engineering (STI), and Lausanne Centre for Ultrafast Science (LACUS), Ecole Polytechnique Fédérale de Lausanne, 1015 Lausanne, Switzerland;* orcid.org/0000-0002-5838-8517

Yujin Tong − *Fritz Haber Institute of the Max Planck Society, 14195 Berlin, Germany; Faculty of Physics, University of Duisburg-Essen, 47057 Duisburg, Germany;* orcid.org/0000-0002-4084-7711

https://dx.doi.org/10.1021/acscatal.0c01177
ACS Catal. 2020, 10, 6084−6093

Sylvie Roke − *Laboratory for Fundamental BioPhotonics, Institutes of Bioengineering (IBI) and Materials Science and Engineering (IMX), School of Engineering (STI), and Lausanne Centre for Ultrafast Science (LACUS), Ecole Polytechnique Fédérale de Lausanne, 1015 Lausanne, Switzerland;* orcid.org/0000-0002-6062-7871

Complete contact information is available at: https://pubs.acs.org/10.1021/acscatal.0c01177

Author Contributions

[‖]G.Z. and I.N. contributed equally to this work.

Notes

The authors declare no competing financial interest.

■ ACKNOWLEDGMENTS

The authors thank Wiebke Frandsen (Inorganic Chemistry department, FHI) and Felix Gerke (Free University of Berlin) for SEM images, the FHI mechanical workshop for production of the electrochemical microscopy cell, Gregor Koch (Inorganic Chemistry department, FHI) for annealing of the polycrystalline gold foils, and Sabine Wasle (Physical Chemistry department, FHI) for the physical vapor deposited samples. This study was supported by the Deutsche Forschungsgemeinschaft (DFG, German Research Foundation) under Germany's Excellence Strategy—EXC-2033—Project no. 390677874, the European Research Council (ERC) under the European Union's Horizon 2020 research and innovation program with Grant agreement no 772286 to RKC and the Marie Skłodowska-Curie grant Agreement no 721766 to I.N. A.M. thanks the Swiss National Science Foundation for funding through the Ambizione Grant PZ00P2_174146.

■ ADDITIONAL NOTES

[a]A similar relative coverage of active sites is expected for different reactions and surfaces because the activity of a particular site is related to the adsorption energy of the reaction intermediate in an exponential fashion: small differences in adsorption energy result in drastic differences in reactivity. The great majority of industrially relevant catalytic materials are not flat, well-defined surfaces. They are rough over multiple length scales with a large range of adsorption sites and energies.[28]

[b]The area that was used to calculate the charge density was 72.8 μm^2 for A and 38.7 μm^2 for B.

■ REFERENCES

(1) Diaz-Morales, O.; Calle-Vallejo, F.; de Munck, C.; Koper, M. T. Electrochemical Water Splitting by Gold: Evidence for an Oxide Decomposition Mechanism. *Chem. Sci.* **2013**, *4*, 2334−2343.

(2) Ertl, G. *Reactions at Solid Surfaces*; John Wiley & Sons, 2009.

(3) Taylor, H. S. Theory of the Catalytic Surface. *Proc. R. Soc. London, Ser. A* **1925**, *108*, 105−111.

(4) Koper, M. T. Structure Sensitivity and Nanoscale Effects in Electrocatalysis. *Nanoscale* **2011**, *3*, 2054−2073.

(5) O'Mullane, A. P. From Single Crystal Surfaces to Single Atoms: Investigating Active Sites in Electrocatalysis. *Nanoscale* **2014**, *6*, 4012−4026.

(6) Farias, M. J.; Feliu, J. M. Determination of Specific Electrocatalytic Sites in the Oxidation of Small Molecules on Crystalline Metal Surfaces. *Top. Curr. Chem.* **2019**, *377*, 5.

(7) Pfisterer, J. H. K.; Liang, Y.; Schneider, O.; Bandarenka, A. S. Direct Instrumental Identification of Catalytically Active Surface Sites. *Nature* **2017**, *549*, 74.

(8) Solla-Gullón, J.; Rodríguez, P.; Herrero, E.; Aldaz, A.; Feliu, J. M. Surface Characterization of Platinum Electrodes. *Phys. Chem. Chem. Phys.* **2008**, *10*, 1359−1373.

(9) Schlögl, R. Heterogeneous Catalysis. *Angew. Chem., Int. Ed.* **2015**, *54*, 3465−3520.

(10) Mariano, R. G.; McKelvey, K.; White, H. S.; Kanan, M. W. Selective Increase in CO_2 Electroreduction Activity at Grain-Boundary Surface Terminations. *Science* **2017**, *358*, 1187−1192.

(11) Warren, S. C.; Voïtchovsky, K.; Dotan, H.; Leroy, C. M.; Cornuz, M.; Stellacci, F.; Hébert, C.; Rothschild, A.; Grätzel, M. Identifying Champion Nanostructures for Solar Water-Splitting. *Nat. Mater.* **2013**, *12*, 842.

(12) Macias-Romero, C.; Nahalka, I.; Okur, H. I.; Roke, S. Optical Imaging of Surface Chemistry and Dynamics in Confinement. *Science* **2017**, *357*, 784−788.

(13) Angerstein-Kozlowska, H.; Conway, B.; Hamelin, A.; Stoicoviciu, L. Elementary Steps of Electrochemical Oxidation of Single-Crystal Planes of Au. Chemical Basis of Processes Involving Geometry of Anions and the Electrode Surfaces. *Electrochim. Acta* **1986**, *31*, 1051−1061.

(14) Angerstein-Kozlowska, H.; Conway, B.; Hamelin, A.; Stoicoviciu, L. Elementary Steps of Electrochemical Oxidation of Single-Crystal Planes of Au Part II. A Chemical and Structural Basis of Oxidation of the (111) Plane. *J. Electroanal. Chem. Interfacial Electrochem.* **1987**, *228*, 429−453.

(15) Zhumaev, U.; Rudnev, A. V.; Li, J.-F.; Kuzume, A.; Vu, T.-H.; Wandlowski, T. Electro-Oxidation of Au(111) in Contact with Aqueous Electrolytes: New Insight from in situ Vibration Spectroscopy. *Electrochim. Acta* **2013**, *112*, 853−863.

(16) Yoshida, K.; Kuzume, A.; Broekmann, P.; Pobelov, I. V.; Wandlowski, T. Reconstruction and Electrochemical Oxidation of Au(110) Surface in 0.1 M H_2SO_4. *Electrochim. Acta* **2014**, *139*, 281−288.

(17) Kondo, T.; Morita, J.; Hanaoka, K.; Takakusagi, S.; Tamura, K.; Takahasi, M.; Mizuki, J.; Uosaki, K. Structure of Au(111) and Au(100) Single-Crystal Electrode Surfaces at Various Potentials in Sulfuric Acid Solution Determined by In Situ Surface X-ray Scattering. *J. Phys. Chem. C* **2007**, *111*, 13197−13204.

(18) Schneeweiss, M.; Kolb, D. Oxide Formation on Au(111): An in situ STM Study. *Solid State Ionics* **1997**, *94*, 171−179.

(19) Weiher, N. Combined In Situ and Ex Situ Studies of an Electrochemical Interface: Investigation of Anodic Oxide Layers on Gold. Ph.D. Thesis, Freie Universitaet Berlin, 2003.

(20) Binninger, T.; Mohamed, R.; Waltar, K.; Fabbri, E.; Levecque, P.; Kötz, R.; Schmidt, T. J. Thermodynamic Explanation of the Universal Correlation between Oxygen Evolution Activity and Corrosion of Oxide Catalysts. *Sci. Rep.* **2015**, *5*, No. 12167.

(21) Xia, S.; Birss, V. A multi-Technique Study of Compact and Hydrous Au Oxide Growth in 0.1 M Sulfuric Acid Solutions. *J. Electroanal. Chem.* **2001**, *500*, 562−573.

(22) Burke, L.; Nugent, P. The Electrochemistry of Gold: II The Electrocatalytic Behaviour of the Metal in Aqueous Media. *Gold Bull.* **1998**, *31*, 39−50.

(23) Wohlfahrt-Mehrens, M.; Heitbaum, J. Oxygen Evolution on Ru and RuO_2 Electrodes Studied using Isotope Labelling and on-line Mass Spectrometry. *J. Electroanal. Chem. Interfacial Electrochem.* **1987**, *237*, 251−260.

(24) Fierro, S.; Nagel, T.; Baltruschat, H.; Comninellis, C. Investigation of the Oxygen Evolution Reaction on Ti/IrO_2 Electrodes Using Isotope Labelling and on-line Mass Spectrometry. *Electrochem. Commun.* **2007**, *9*, 1969−1974.

(25) Macounova, K.; Makarova, M.; Krtil, P. Oxygen Evolution on Nanocrystalline RuO_2 and $Ru_{0.9}Ni_{0.1}O_{2-\delta}$ Electrodes-DEMS Approach to Reaction Mechanism Determination. *Electrochem. Commun.* **2009**, *11*, 1865−1868.

(26) McCrory, C. C.; Jung, S.; Peters, J. C.; Jaramillo, T. F. Benchmarking Heterogeneous Electrocatalysts for the Oxygen Evolution Reaction. *J. Am. Chem. Soc.* **2013**, *135*, 16977−16987.
(27) Macias-Romero, C.; Didier, M. E.; Jourdain, P.; Marquet, P.; Magistretti, P.; Tarun, O. B.; Zubkovs, V.; Radenovic, A.; Roke, S. High Throughput Second Harmonic Imaging for Label-Free Biological Applications. *Opt. Express* **2014**, *22*, 31102−31112.
(28) Somorjai, G. A. Modern Surface Science and Surface Technologies: An Introduction. *Chem. Rev.* **1996**, *96*, 1223−1236.
(29) Burke, L. D.; Collins, J. A.; Murphy, M. A. Redox and Electrocatalytic Activity of Copper in Base at Unusually Low, Premonolayer Potentials. *J. Solid State Electrochem.* **1999**, *4*, 34−41.
(30) Declan Burke, D.; O'Mullane, A. P. Generation of Active Surface States of Gold and the Role of such States in Electrocatalysis. *J. Solid State Electrochem.* **2000**, *4*, 285−297.
(31) Burke, L.; Ahern, A.; O'Mullane, A. High Energy States of Gold and their Importance in Electrocatalytic Processes at Surfaces and Interfaces. *Gold Bull.* **2002**, *35*, 3−10.
(32) Luo, L.; White, H. S. Electrogeneration of Single Nanobubbles at Sub-50-nm-Radius Platinum Nanodisk Electrodes. *Langmuir* **2013**, *29*, 11169−11175.
(33) Chen, Q.; Wiedenroth, H. S.; German, S. R.; White, H. S. Electrochemical Nucleation of Stable N_2 Nanobubbles at Pt Nanoelectrodes. *J. Am. Chem. Soc.* **2015**, *137*, 12064−12069.
(34) Chen, Q.; Luo, L.; White, H. S. Electrochemical Generation of a Hydrogen Bubble at a Recessed Platinum Nanopore Electrode. *Langmuir* **2015**, *31*, 4573−4581.
(35) Ren, H.; German, S. R.; Edwards, M. A.; Chen, Q.; White, H. S. Electrochemical Generation of Individual O_2 Nanobubbles via H_2O_2 Oxidation. *J. Phys. Chem. Lett.* **2017**, *8*, 2450−2454.
(36) German, S. R.; Edwards, M. A.; Ren, H.; White, H. S. Critical Nuclei Size, Rate, and Activation Energy of H_2 Gas Nucleation. *J. Am. Chem. Soc.* **2018**, *140*, 4047−4053.
(37) Chen, Q.; Luo, L.; Faraji, H.; Feldberg, S. W.; White, H. S. Electrochemical Measurements of Single H_2 Nanobubble Nucleation and Stability at Pt Nanoelectrodes. *J. Phys. Chem. Lett.* **2014**, *5*, 3539−3544.
(38) Westerheide, D.; Westwater, J. Isothermal Growth of Hydrogen Bubbles During Electrolysis. *AIChE J.* **1961**, *7*, 357−362.
(39) Glas, J.; Westwater, J. Measurements of the Growth of Electrolytic Bubbles. *Int. J. Heat Mass Transfer* **1964**, *7*, 1427−1443.
(40) Seddon, J. R.; Kooij, E. S.; Poelsema, B.; Zandvliet, H. J.; Lohse, D. Surface Bubble Nucleation Stability. *Phys. Rev. Lett.* **2011**, *106*, No. 056101.
(41) Guan, M.; Guo, W.; Gao, L.; Tang, Y.; Hu, J.; Dong, Y. Investigation on the Temperature Difference Method for Producing Nanobubbles and Their Physical Properties. *ChemPhysChem* **2012**, *13*, 2115−2118.
(42) Zambelli, T.; Wintterlin, J.; Trost, J.; Ertl, G. Identification of the "Active Sites" of a Surface-Catalyzed Reaction. *Science* **1996**, *273*, 1688−1690.
(43) Dahl, S.; Logadottir, A.; Egeberg, R.; Larsen, J.; Chorkendorff, I.; Törnqvist, E.; Nørskov, J. K. Role of Steps in N_2 Activation on Ru(0001). *Phys. Rev. Lett.* **1999**, *83*, 1814.
(44) Amakawa, K.; Wrabetz, S.; Kröhnert, J.; Tzolova-Müller, G.; Schlögl, R.; Trunschke, A. In Situ Generation of Active Sites in Olefin Metathesis. *J. Am. Chem. Soc.* **2012**, *134*, 11462−11473.
(45) Plowman, B. J.; O'Mullane, A. P.; Bhargava, S. K. The Active Site Behaviour of Electrochemically Synthesised Gold Nanomaterials. *Faraday Discuss.* **2011**, *152*, 43−62.
(46) Cherevko, S.; Kulyk, N.; Chung, C.-H. Utilization of Surface Active Sites on Gold in Preparation of Highly Reactive Interfaces for Alcohols Electrooxidation in Alkaline Media. *Electrochim. Acta* **2012**, *69*, 190−196.
(47) Plowman, B. J.; Field, M. R.; Bhargava, S. K.; O'Mullane, A. P. Exploiting the Facile Oxidation of Evaporated Gold Films to Drive Electroless Silver Deposition for the Creation of Bimetallic Au/Ag Surfaces. *ChemElectroChem* **2014**, *1*, 76−82.
(48) Hansen, P. L.; Wagner, J. B.; Helveg, S.; Rostrup-Nielsen, J. R.; Clausen, B. S.; Topsøe, H. Atom-Resolved Imaging of Dynamic Shape Changes in Supported Copper Nanocrystals. *Science* **2002**, *295*, 2053−2055.
(49) Lunkenbein, T.; Schumann, J.; Behrens, M.; Schlögl, R.; Willinger, M. G. Formation of a ZnO Overlayer in Industrial Cu/ZnO/Al_2O_3 Catalysts Induced by Strong Metal-Support Interactions. *Angew. Chem.* **2015**, *127*, 4627−4631.
(50) Guyot-Sionnest, P.; Tadjeddine, A. Study of Ag(111) and Au(111) Electrodes by Optical Second-Harmonic Generation. *J. Chem. Phys.* **1990**, *92*, 734−738.
(51) Baten, S. M.; Taylor, A. G.; Wilde, C. P. Second Harmonic Generation Studies of the Oxidation of Metal Electrodes: Compact and Hydrous Oxide Growth at Gold Electrodes in Acid Solutions. *Electrochim. Acta* **2008**, *53*, 6829−6834.
(52) Wieckowski, A. *Interfacial Electrochemistry*; Marcel Dekker Inc., 1999.
(53) Ruettinger, W.; Ilinich, O. *Encyclopedia of Chemical Processing*; Taylor & Francis, 2006; Vol. 5.
(54) Cherevko, S.; Topalov, A. A.; Zeradjanin, A. R.; Katsounaros, I.; Mayrhofer, K. J. Gold Dissolution: Towards Understanding of Noble Metal Corrosion. *RSC Adv.* **2013**, *3*, 16516−16527.
(55) Burke, L.; Cunnane, V.; Lee, B. Unusual Postmonolayer Oxide Behavior of Gold Electrodes in Base. *J. Electrochem. Soc.* **1992**, *139*, 399−406.
(56) Zeng, K.; Zhang, D. Recent Progress in Alkaline Water Electrolysis for Hydrogen Production and Applications. *Prog. Energy Combust. Sci.* **2010**, *36*, 307−326.
(57) Zwaschka, G.; Wolf, M.; Campen, R. K.; Tong, Y. A Microscopic Model of the Electrochemical Vibrational Stark Effect: Understanding VSF Spectroscopy of (bi)Sulfate on Pt(111). *Surf. Sci.* **2018**, *678*, 78−85.
(58) Eggen, P.-O. A Simple Hydrogen Electrode. *J. Chem. Educ.* **2009**, *86*, 352.

https://dx.doi.org/10.1021/acscatal.0c01177
ACS Catal. 2020, 10, 6084−6093